**Electronic Supplementary Information (ESI)**

# Promising Thermoelectric Performance in Earth Abundant SnS: Local Sn Distortion and Modular Misfit Nanostructures

Riddhimoy Pathak[a], Shuva Biswas[a], Swagata Patra[a], & Kanishka Biswas[a,b,*]

[a]*New Chemistry Unit, Jawaharlal Nehru Centre for Advanced Scientific Research (JNCASR), Jakkur P.O., Bangalore 560064, India*
[b]*School of Advanced Materials and International Centre of Materials Science, Jawaharlal Nehru Centre for Advanced Scientific Research (JNCASR), Jakkur P.O., Bangalore 560064, India.*
**kanishka@jncasr.ac.in*

**Methods.**

**Reagents.** Tin (Sn, Strategy Elements, 99.999 %) and Sulphur (S, Alfa Aesar, 99.99 %) were used for the synthesis of all the compounds.

**Synthesis.** High-quality crystalline ingots (~6 g) of $Sn_{1-x}S$ (x = 0–0.02) were synthesized by combining appropriate ratios of high-purity Sn and S in a quartz tube. The tubes were sealed under vacuum ($10^{-5}$ Torr), then gradually heated to 673 K over 20 hours and annealed for 36 hours. Subsequently, they were heated to 1223 K over 4 hours, annealed for 10 hours, and slowly cooled to room temperature over 12 hours. To ensure phase homogenization, the ingots were further annealed at 873 K for 6 hours multiple times, followed by furnace cooling to room temperature. The resulting shiny, high-quality polycrystalline ingots of $Sn_{1-x}S$ (x = 0.00–0.02) were ground into fine powders, which were loaded into a 10 mm diameter graphite die. These powders, enclosed in the die, were placed between electrodes in a spark plasma sintering system (SPS211-LX, Dr. Sinter Lab). After creating a vacuum, the powders were consolidated into cylindrical shapes at 873 K for 8 minutes under an axial pressure of 50 MPa. The sintered cylindrical samples were then cut into coin and bar shapes (Figure S6, SI), polished, and prepared for thermal and electrical transport measurements.

**Powder X-ray Diffraction.** Room-temperature powder X-ray diffraction (PXRD) patterns for all samples of $Sn_{1-x}S$ (x = 0-0.02) were collected using a Rigaku SmartLab SE diffractometer with Cu Kα radiation (λ = 1.5406 Å).

**Electrical Transport.** An ULVAC-RIKO ZEM-3 instrument was used for the simultaneous measurements of electrical conductivity and Seebeck coefficient from room temperature to 873 K for $Sn_{1-x}S$ (x = 0.00-0.02) under He atmosphere. The typical samples had a parallelepiped shape of dimensions of ~2.5 × 2.5 × 8.5 $mm^3$. The electrical and thermal transport were measured in the same direction.

**Thermal Transport.** The thermal diffusivity (D) of the samples was measured using the laser flash diffusivity method with a Netzsch LFA-457 system, within the temperature range of 300–873 K under a nitrogen atmosphere. Coin-shaped specimens with a diameter of approximately 10 mm and a thickness less than ~2 mm were used for the measurements. The temperature-dependent heat capacity ($C_p$) of SnS was determined by comparison with a standard sample (pyroceram)

using the same LFA-457 system. The total thermal conductivity ($\kappa_{tot}$) was estimated using the formula $\kappa_{tot} = D\rho C_p$, where $\rho$ represents the density of the samples, which was found to be ~97% of the theoretical value. The error in thermal conductivity measurement in Netzsch LFA-457 is ~5%.

**Lorenz number calculation.** $\kappa_{lat}$ is estimated by subtracting the $\kappa_{ele} = L\sigma T$ from total $\kappa$. The Lorenz number (L) is determined by fitting the reduced chemical potential derived from the temperature-dependent Seebeck coefficient data, given by the following equations:

$$S = \frac{k_B}{e}\left(\frac{2F_1(\eta)}{F_0(\eta)} - \eta\right),$$

and $L = \left(\frac{k_B}{e}\right)^2 \left(\frac{3F_0(\eta)F_2(\eta) - 4F_1^2(\eta)}{F_0^2(\eta)}\right)$,

where $\eta = \frac{E_F}{k_B T}$ and the Fermi integral $F_n(\eta)$ is defined as:

$$F_n(\eta) = \int_0^\infty \frac{\varepsilon^n}{1+e^{\varepsilon-\eta}}$$

**Hall measurement:** Room-temperature carrier concentrations were determined from Hall coefficient measurements using an instrument developed by Excel Instrument, India. A maximum magnetic field of 1 T was applied during the measurements. The carrier concentration at room temperature was estimated using the formula, $n = 1/e.R_H$ where $e$ is the electronic charge and $R_H$ is the Hall coefficient.

**Diffuse reflectance.** The diffuse reflectance of the sample was recorded using a PerkinElmer, Lambda-900 UV/Vis/near-IR spectrometer in reflectance mode in the range of 250-800 nm. The absorption data ($\alpha/\Lambda$) of $Sn_{1-x}S$ (x = 0.00-0.02) was assessed from reflectance data employing the Kubelka–Munk equation; $\alpha/\Lambda = (1-R)^2/(2R)$; where R, $\alpha$, and $\Lambda$ indicate reflectance, absorption, and scattering coefficients, respectively.

**X-ray photoelectron spectroscopy (XPS).** XPS measurement was carried out using an Omicron nanotechnology spectrometer with an Al-K$\alpha$ (1487.6 eV) X-ray source.

**Field emission scanning electron microscopy (FESEM).** FESEM images were taken using Apero 2 S Field emission scanning electron microscope in backscattered electron (BSE) modes having an accelerated voltage range of 200 V – 30 kV.

**Transmission electron microscopy (TEM).** The sample was dispersed in ethanol and drop casted on a carbon (Holey Carbon, 200 mesh) coated Cu TEM grid. The TEM and HRTEM images were taken using a JEOL (JEM-F200) instrument (operating at 200 kV).

**Sound velocity measurement.** The longitudinal ($v_l$) and transverse ($v_t$) sound velocities were estimated on a coin-shaped sintered material by using an Epoch 650 Ultrasonic Flaw Detector (Olympus) instrument with the transducer frequency of 5 MHz. The mean sound velocity ($v_m$) was estimated using the formula: $v_m = \left(\frac{3}{v_l^{-3}+2v_t^{-3}}\right)^{\frac{1}{3}}$ where $v_l$ and $v_t$ denotes longitudinal and transverse sound velocity respectively. The bulk and shear modulus of the system were further calculated from the sound velocity data by using the formula : $G = v_t^2\rho$ and $B = v_l^2\rho - \frac{4}{3}v_t^2\rho$ where, B and G are the bulk and shear moduli respectively. ρ refers to the density of the sample. The Poisson's ratio $\nu$ can be expressed in terms of the longitudinal ($v_l$) and transverse ($v_t$) sound velocities as: $\nu = \frac{v_l^2-2v_t^2}{2(v_l^2-v_t^2)}$ . The Grüneisen parameter (γ) is calculated from the elastic properties using the formula[1] $\gamma = \frac{3}{2}\left(\frac{1+\nu}{2-3\nu}\right)$.

**Synchrotron X-ray pair distribution function analysis:** X-ray Pair Distribution Function (X-PDF) experiment was carried out for the pristine SnS sample at the P02.1 beamline of PETRA III, DESY, Germany.[2] The finely grounded powdered sample was loaded into a capillary tube of 0.8 mm diameter, and then flame sealed the open side of the capillary. The sample-loaded capillary was mounted on the sample holder, which was positioned between the X-ray source and the Varex detector. The distance between the detector and the sample was kept around 300 mm. X-ray of fixed energy 59.798 keV (λ = 0.207337 Å) was used, and the data was collected at room temperature. Lanthanum Hexaboride ($LaB_6$) was used as a calibration standard. DAWN Science software was employed to integrate the raw data and obtain the scattering intensities in Q-space.[3]These intensities were normalized and corrected for secondary effects using PDFgetX3 before being Fourier transformed to acquire the atomic pair distribution function, G(r)[4].

Via Fourier transformation of scattering structure function F(Q) we got the G(r), which is the probability of finding nearest neighbour bonding at a distance r for a particular material as shown here

$$\mathrm{G(r)} = \frac{2}{\pi} \int_{Q_{min}}^{\infty} F(Q)\, Sin(Qr)\, dQ$$

where Q denotes the momentum transfer of the scattering particle. We have derived F(Q) from the scattering data which is related to the structure-function S(Q) by the equation F(Q) = Q[S(Q)-1]. The following parameters we have used for the data conversion as $Q_{min}$ = 1 Å$^{-1}$, $Q_{max}$ = 23 Å$^{-1}$, $r_{min}$ = 2.2 Å, $r_{max}$ = 30 Å and $r_{poly}$ = 0.9.

PDFgui software was used to fit and model the final data[5] considering a tetragonal *Pnma* structural model. Lattice parameters, scale factor, linear atomic correlation factor, thermal displacement parameters, and the allowed positions were refined for global structure modelling (r = 2.2-30 Å). Whereas simulation of the undistorted local structure (r = 2.2-3.75 Å) was performed by fixing the lattice position and thermal parameters. For the distorted model, we have refined the lattice parameters, scale factor, and, finally, atomic displacement parameters of Sn atoms to improve the overall fitting.

**Thermoelectric device fabrication**. The single-leg thermoelectric device was fabricated by consolidating $Sn_{0.985}S$ powder along with end layers of (Ni+Fe)/Cu using spark plasma sintering (SPS) at 873 K under an applied pressure of 48 MPa for 5 min under vacuum. The mixture of (Ni+Fe) layers served as diffusion barriers, while Cu was used to ensure good electrical contact with the external Cu plates, thereby minimizing interfacial resistance. The sintered device was subsequently integrated into the measurement setup, where the electrical connections were completed using a conductive epoxy layer[6]. A schematic of the device is shown in Fig. S20. Power generating properties of the fabricated device was estimated by mini-PEM module testing system (Advance Riko)[6, 7]. However, Mini-PEM module does not offer appropriate shield to control the radiative heat loss, hence the heat flow through the device is substantially overestimated. Thus, the total amount of heat flow ($Q_c$) was estimated using the Fourier Law[8] which can be written as:

$$Q_C = \frac{\kappa(T_{avg}) * A * \Delta T}{L}$$

where A is the total cross-sectional area and L is the length of the fabricated single-leg device. In addition, $\kappa(T_{avg})$ is the thermal conductivity of the single leg at $T_{avg} = (T_h + T_c)/2$, and $\Delta T = T_h - T_c$ where $T_h$ and $T_c$ are the temperatures at the hot and cold end respectively. The efficiency was calculated by the ratio of output power ($P_{out}$) of the thermoelectric device and the total amount of heat flow.

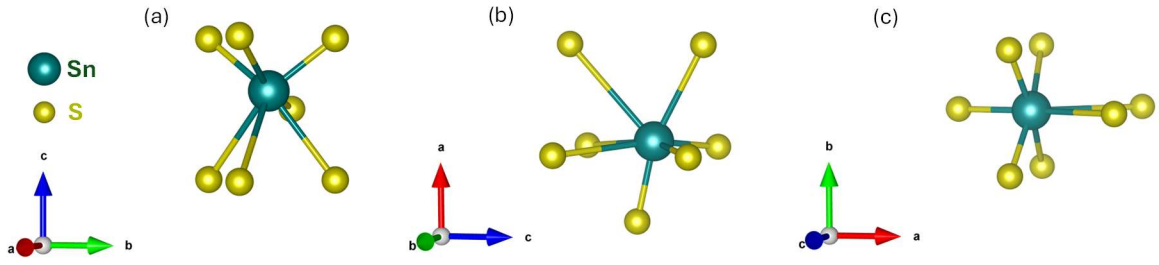


**Fig. S1.** Hepta-coordination of SnS viewed along the three crystallographic directions.

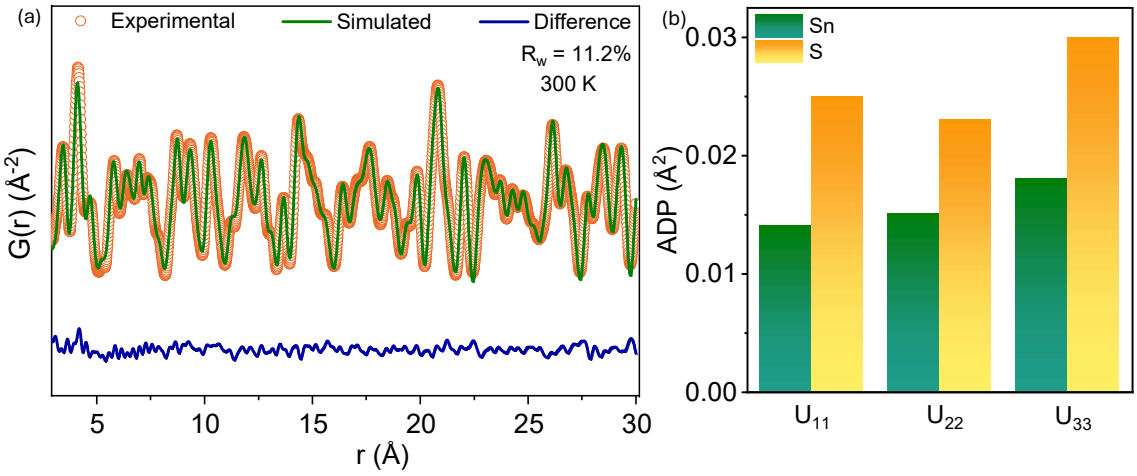


**Fig. S2.** (a) Room temperature average structure *G(r)* (r = 2.78-30 Å) plot of SnS. (b) Atomic displacement parameters of Sn and S along crystallographic *a* ($U_{11}$), *b* ($U_{22}$) and *c* ($U_{33}$) directions.

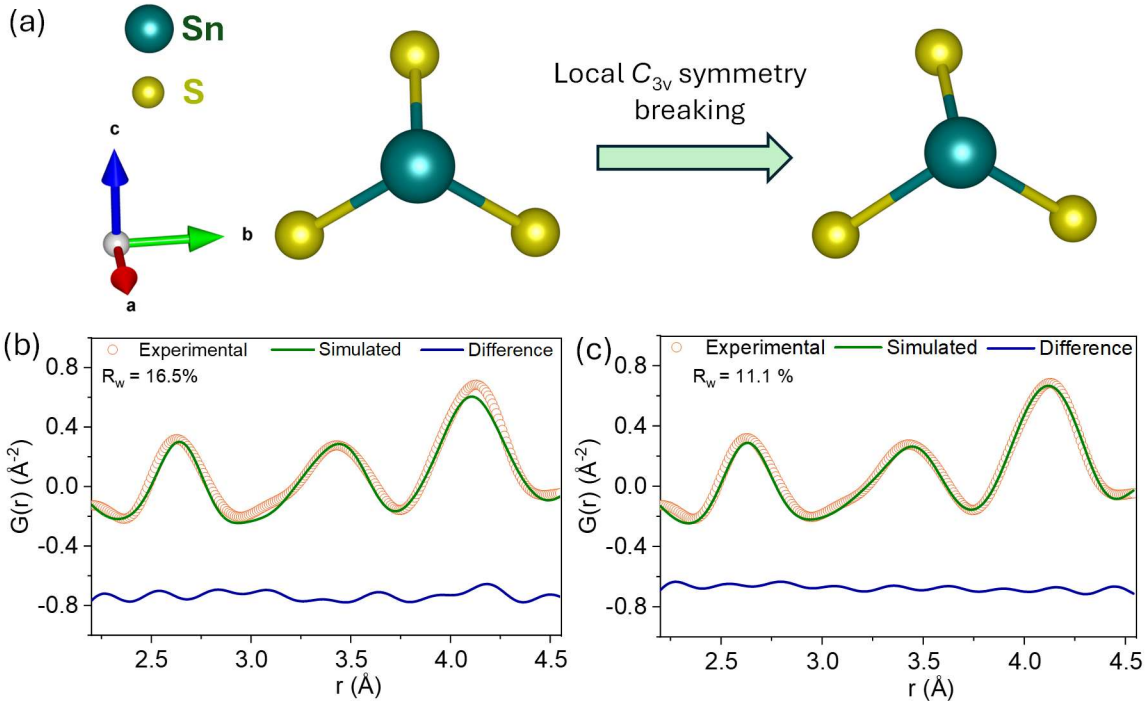


**Fig. S3.** (a) Local $C_{3v}$ breaking due to Sn off-centering in SnS. Local structural fit of the *G(r)* plot considering the first three peaks (b) before and (c) after local Sn distortion.

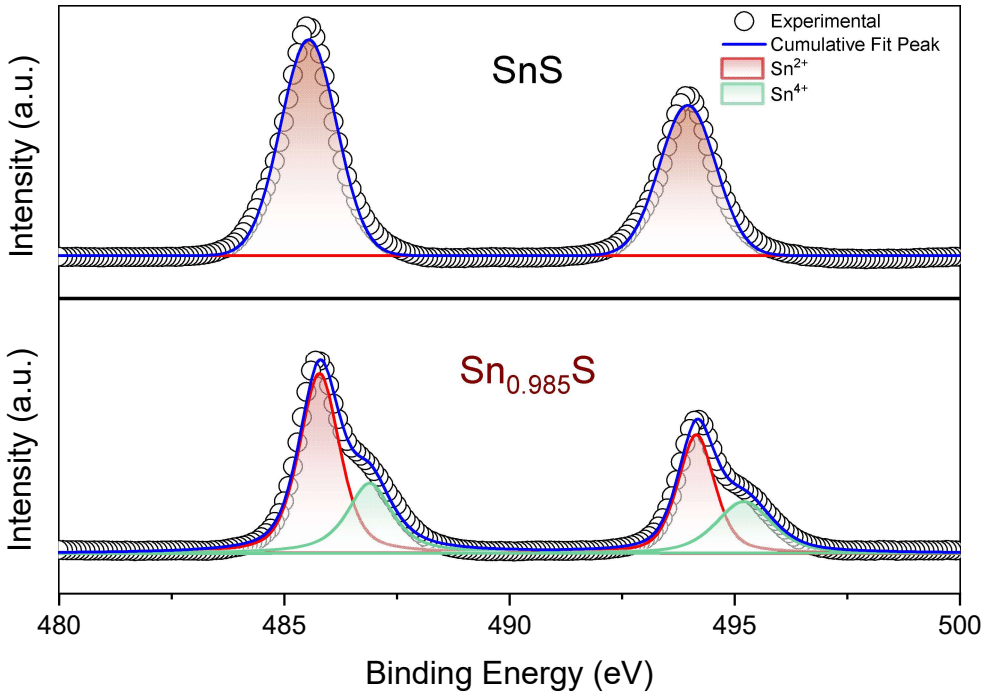


**Fig. S4.** Comparative X-ray photoelectron spectroscopy (XPS) of SnS and $Sn_{0.985}S$.

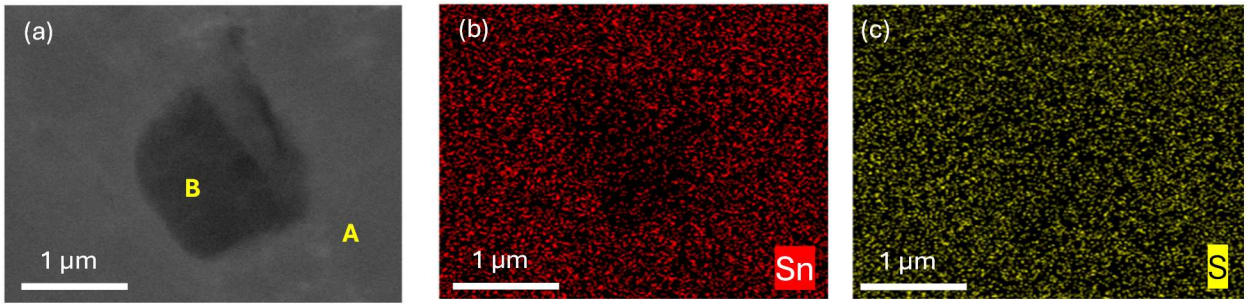


**Fig. S5.** (a) FESEM-BSE image of $Sn_{0.985}S$ with corresponding EDAX elemental color mapping of (b) Sn and (c) S.

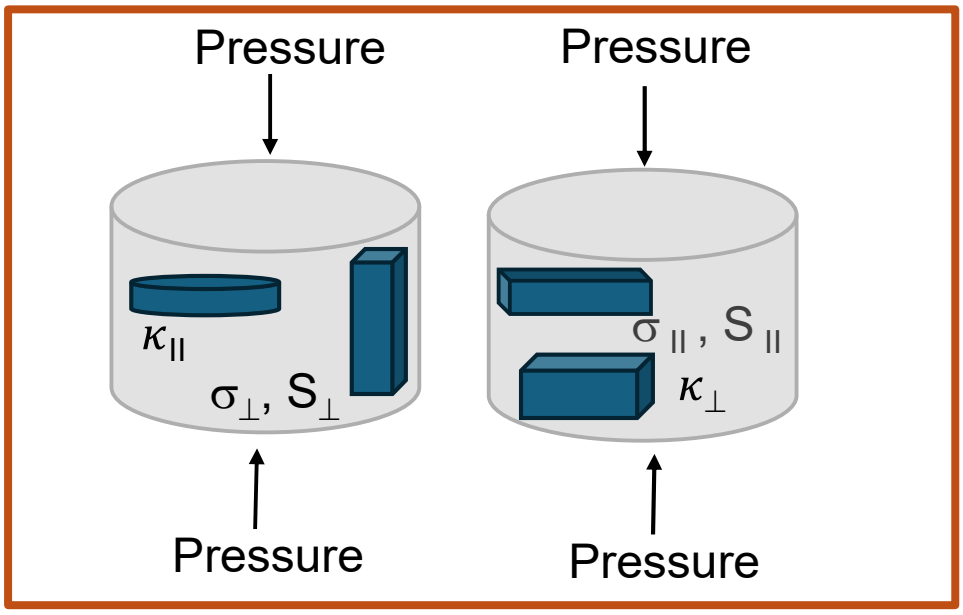


**Fig. S6.** Illustration showing pressing directions of spark plasma sintering (SPS) and corresponding anisotropic measurement of $Sn_{1-x}S$.

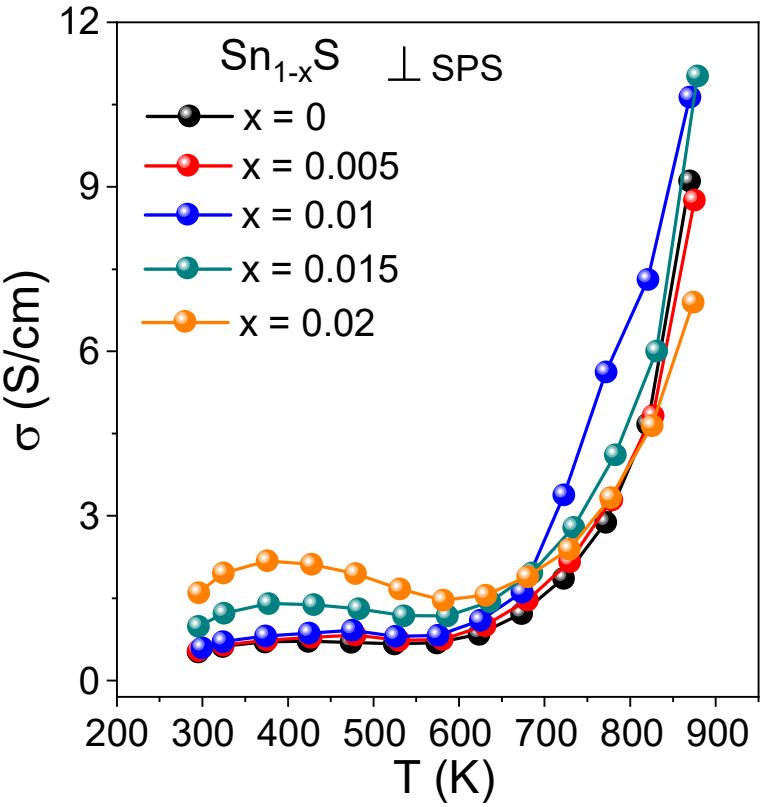


**Fig. S7.** Temperature variation of electrical conductivity (σ) of $Sn_{1-x}S$ (x = 0-0.02) perpendicular to the SPS direction.

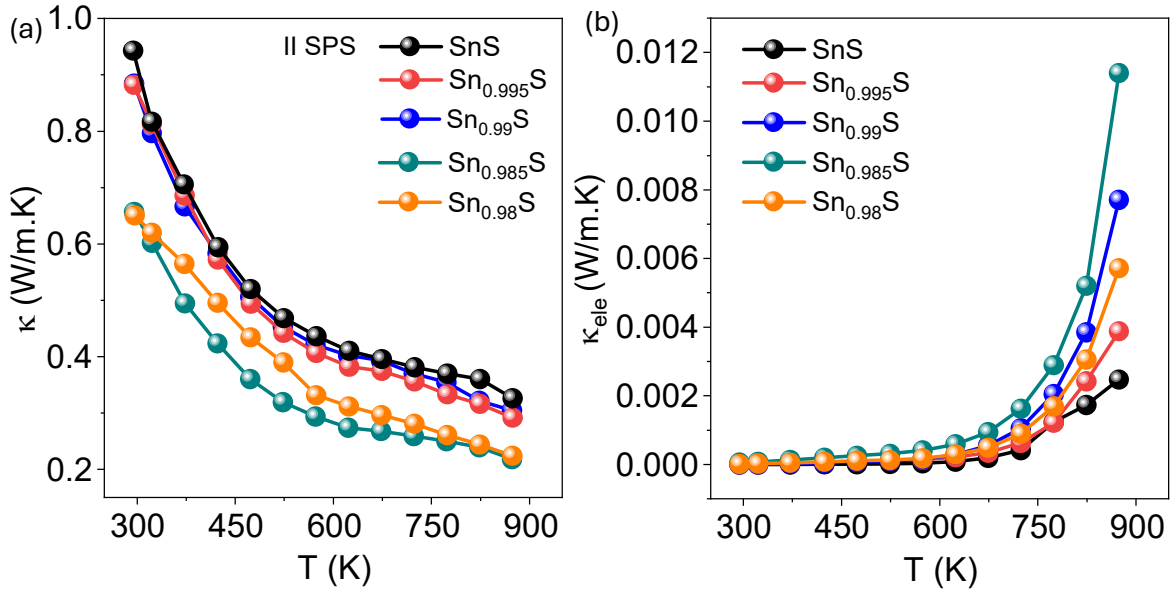


**Fig. S8.** Temperature variation of (a) total thermal conductivity (κ) and (b) electrical thermal conductivity ($\kappa_{ele}$) of $Sn_{1-x}S$ (x = 0-0.02) parallel to the SPS direction.

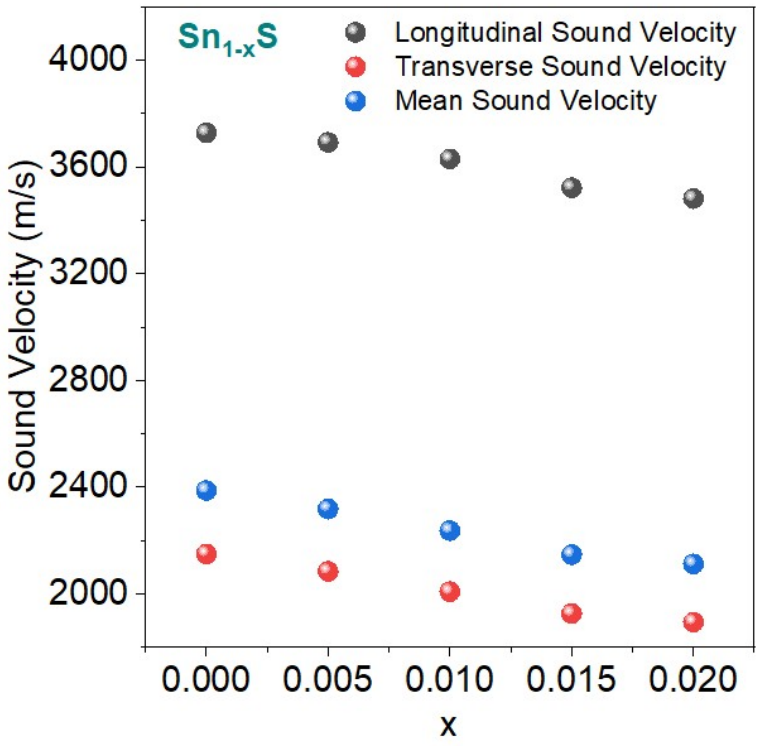


**Fig. S9.** Room temperature sound velocity of $Sn_{1-x}S$.

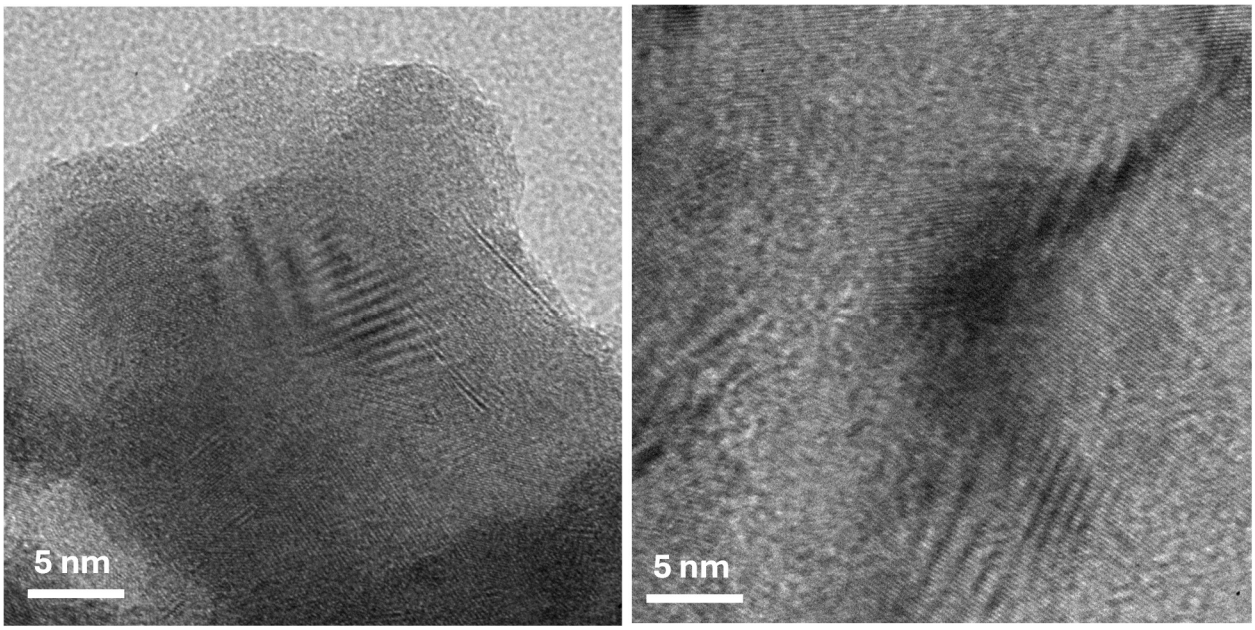


**Fig. S10.** TEM images of $Sn_{1-x}S$ showing ripple-like modulations.

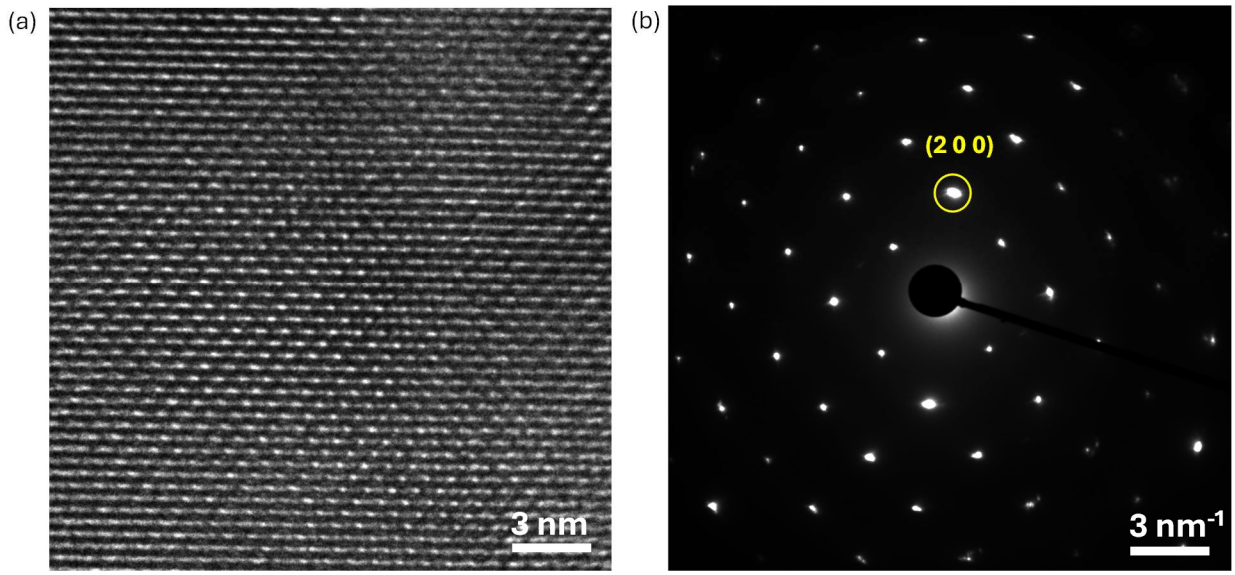


**Fig. S11.** (a) HRTEM image and corresponding (b) SAED of pristine SnS.

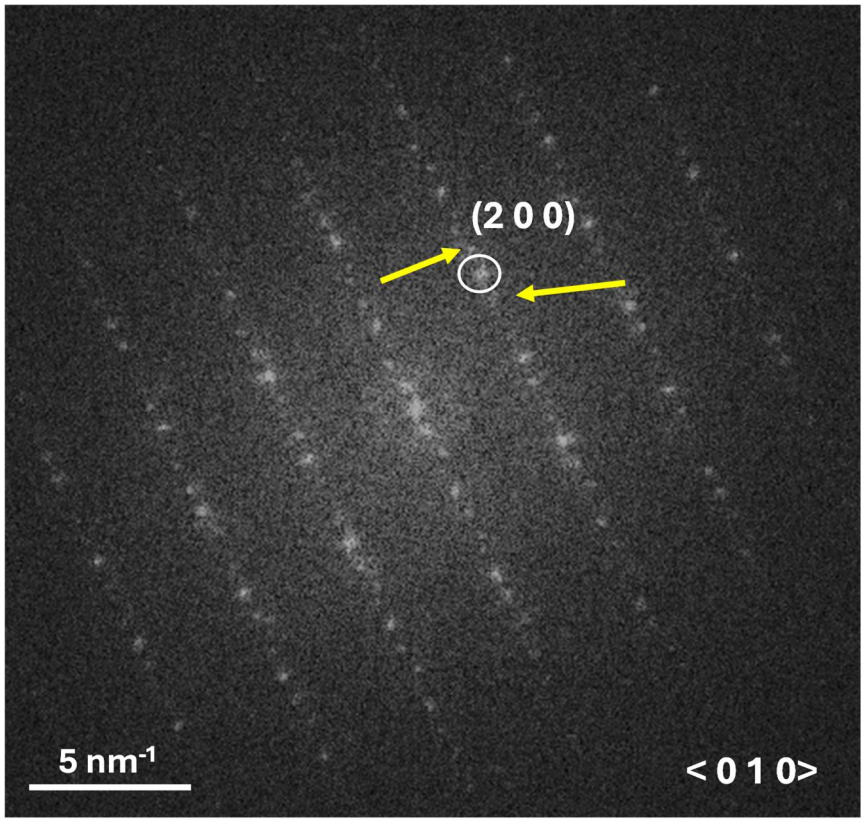


**Fig. S12**. Fast Fourier transformation (FFT) image of Figure 3d, main manuscript showing splitting of primary diffraction spot.

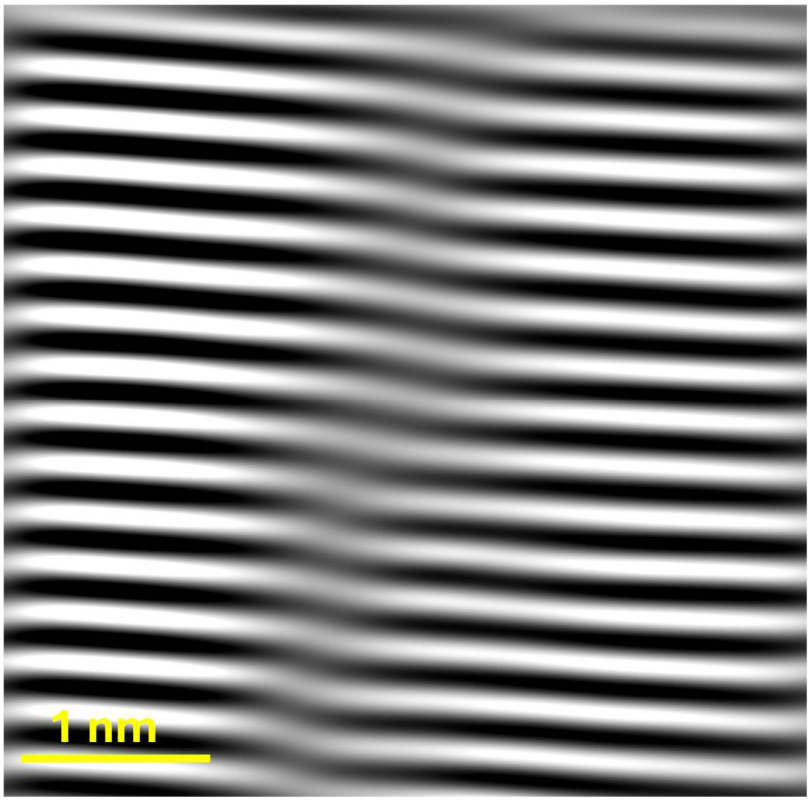


**Fig. S13.** IFFT image of Fig 3e main manuscript showing line defects in $Sn_{0.985}S$.

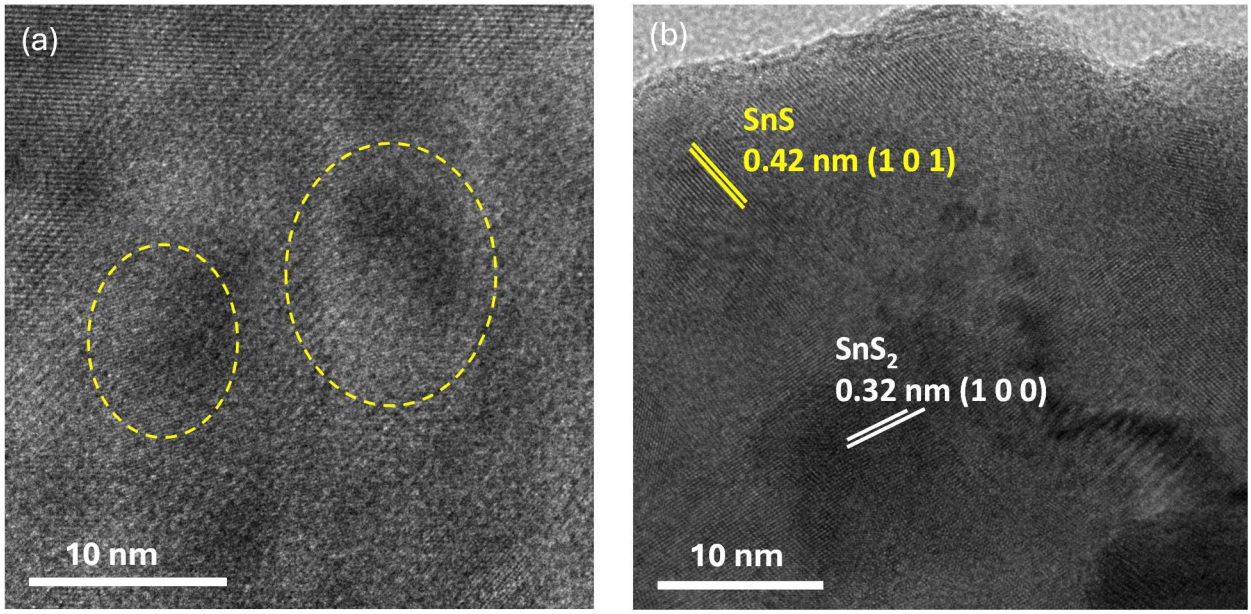


**Fig. S14.** (a) Low and (b) high magnification TEM image $Sn_{0.985}S$ matrix showing embedded $SnS_2$ nanoprecipitates.

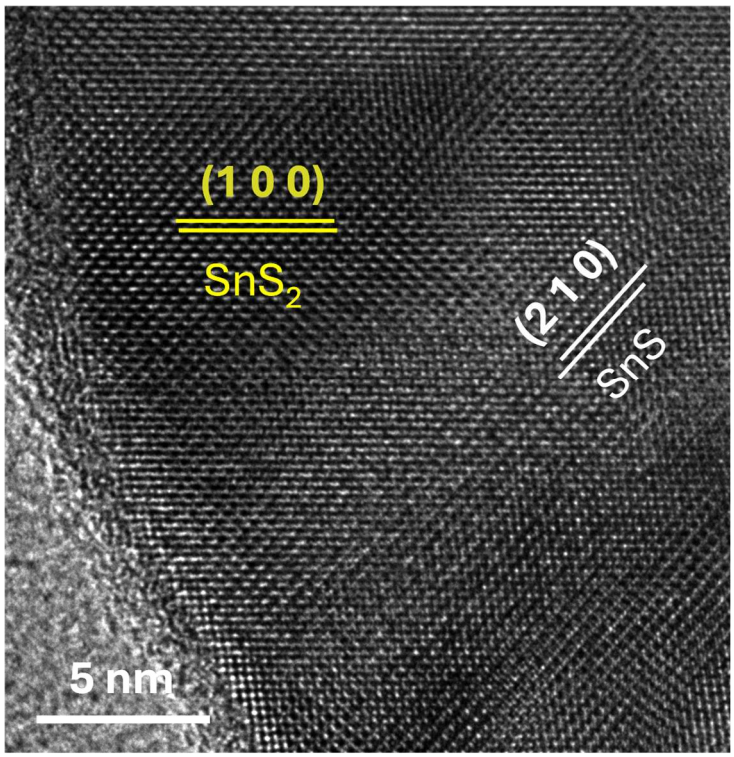


**Fig. S15.** HRTEM image $Sn_{0.985}S$ matrix showing embedded $SnS_2$ nanoprecipitates.

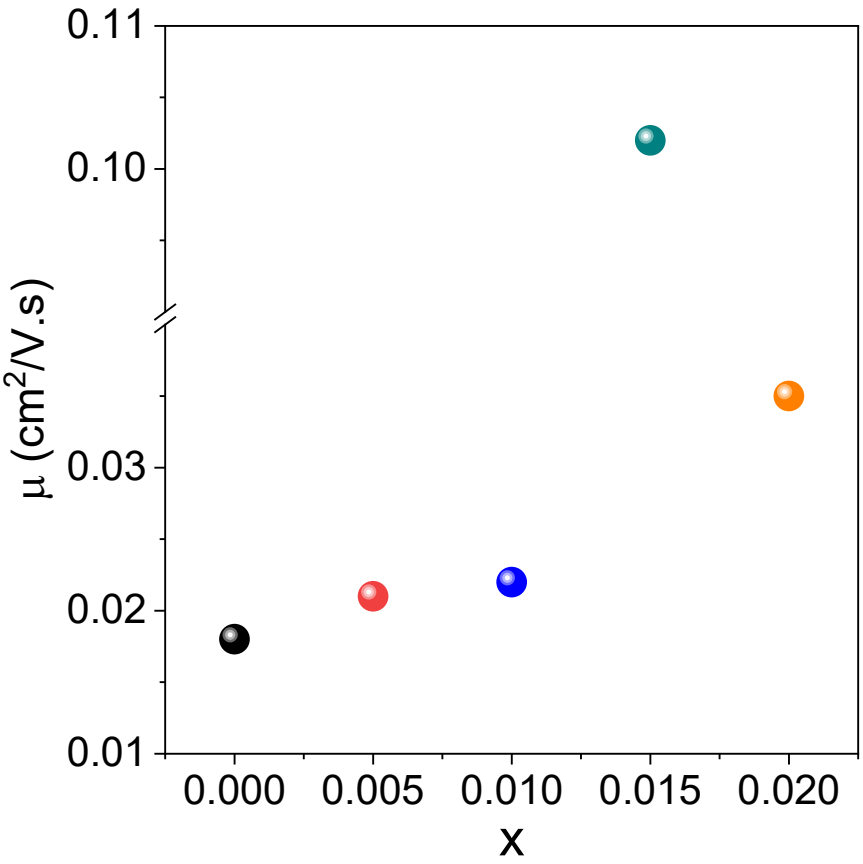


**Fig. S16.** Room temperature carrier mobility of $Sn_{1-x}S$ (x=0-0.02).

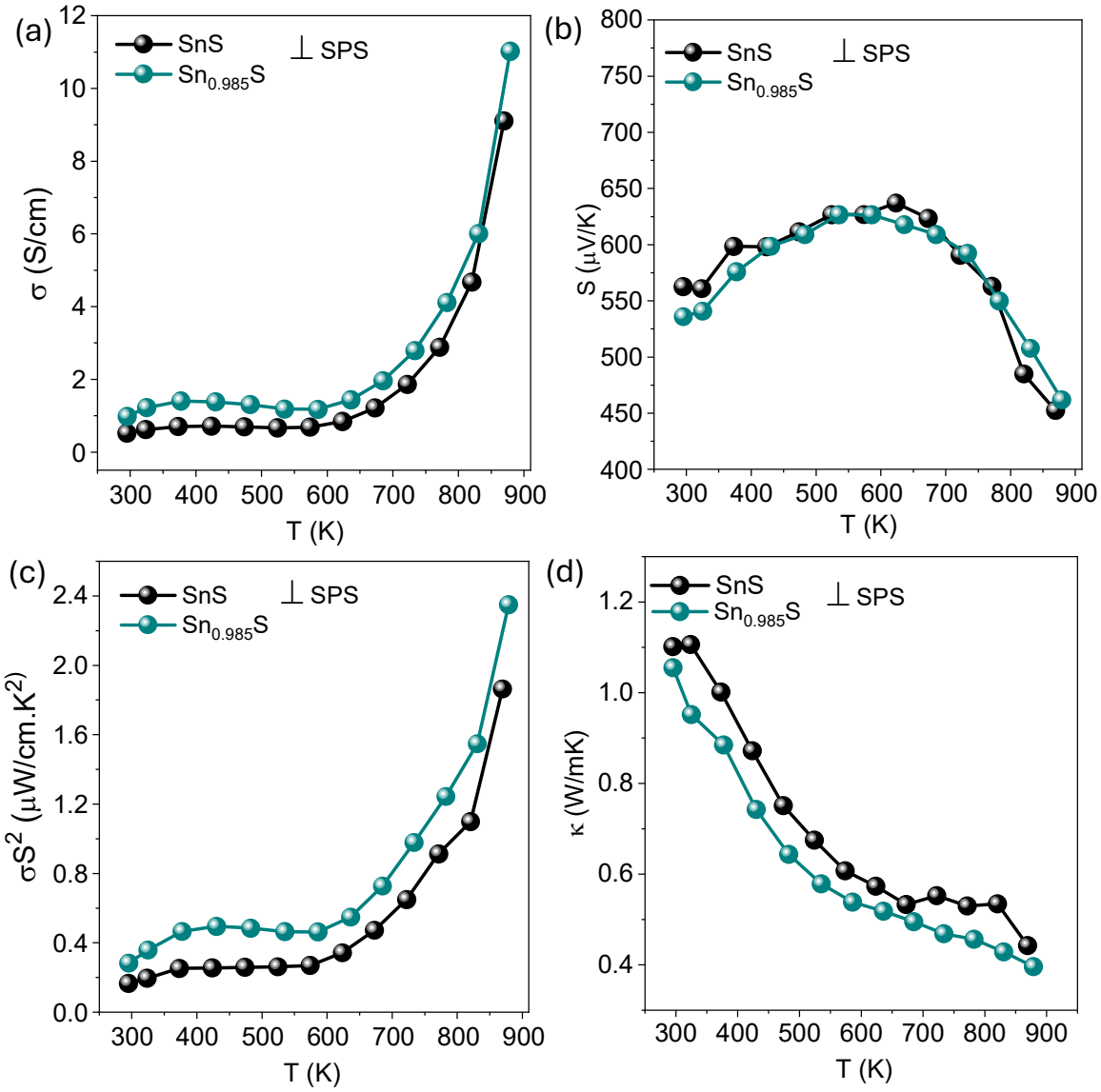


**Fig. S17.** Temperature variation of (a) electrical conductivity, (b) Seebeck co-efficient, (c) power factor, and (d) total thermal conductivity of $Sn_{1-x}S$ (x = 0-0.02) perpendicular to the SPS direction

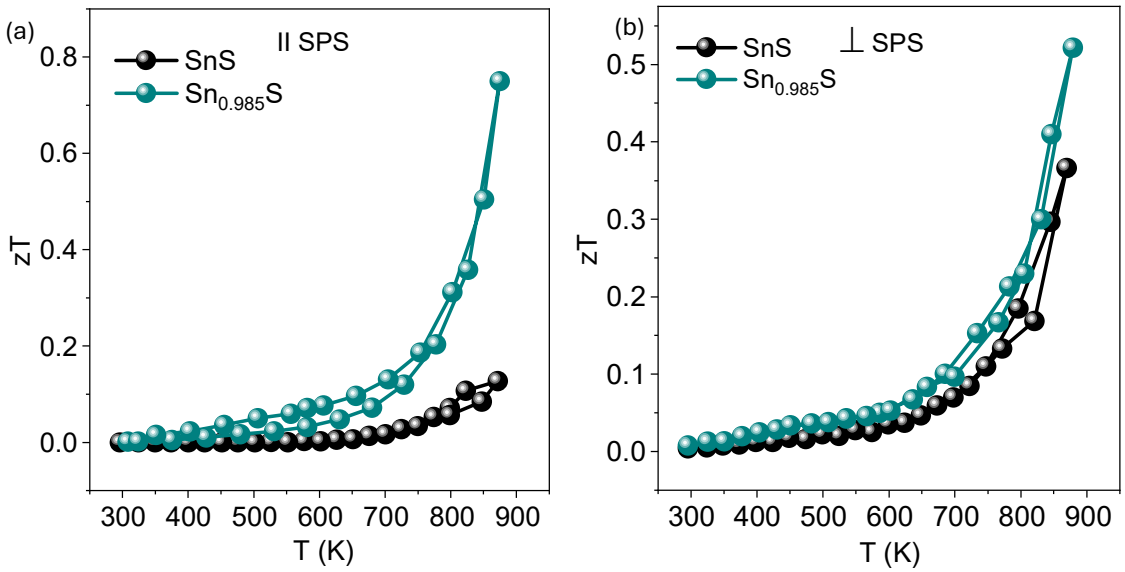


**Fig. S18.** Reversibility of figure of merit (zT) of SnS and $Sn_{0.985}S$ (a) parallel and (b) perpendicular to the SPS direction

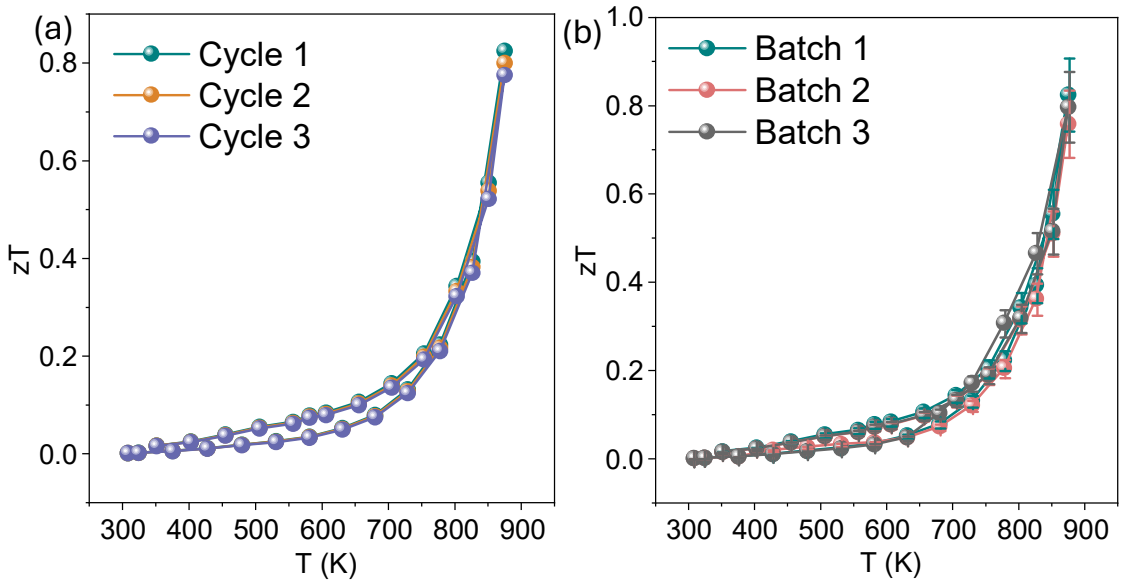


**Fig. S19.** (a) Cyclability and (b) reproducibility of figure of merit (zT) of $Sn_{0.985}S$ parallel to the SPS direction.

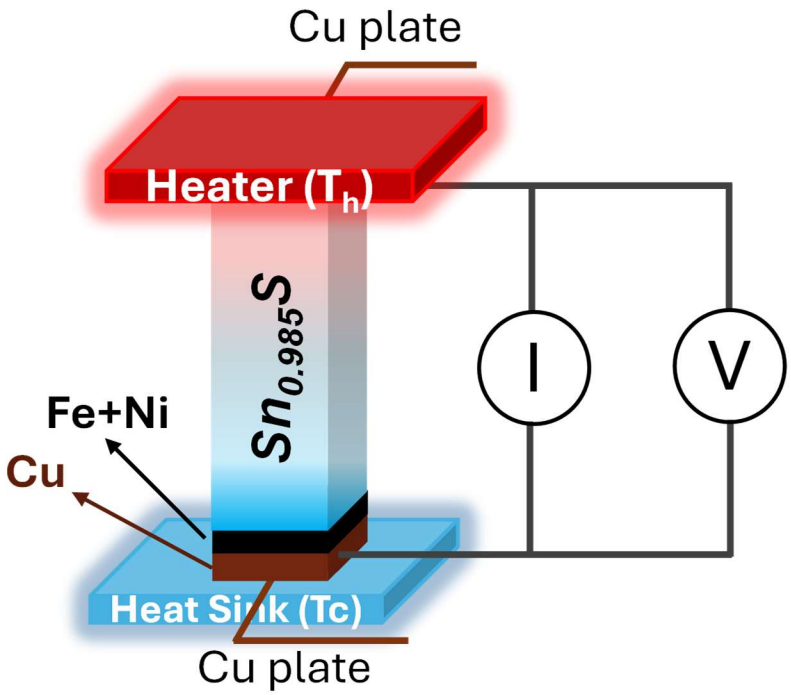


**Fig. S20.** A schematic of single-leg thermoelectric device based on $Sn_{0.985}S$ showing heater, heat sink, thermoelectric material pressed along with a mixture of Fe and Ni as a diffuson layer and Cu used for a better contact with Cu plate minimizing contact resistance.

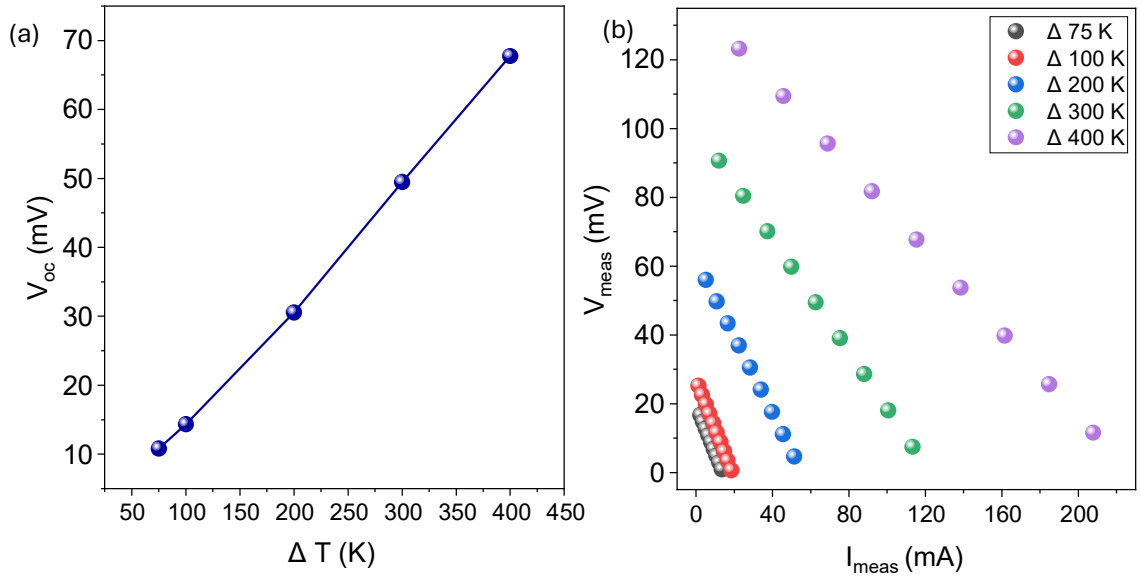


**Fig. S21.** Variation of open circuit voltage ($V_{oc}$) with ΔT and (b) current-dependent output voltage ($V_{meas}$) at different ΔT. of single leg thermoelectric device based on $Sn_{0.985}S$

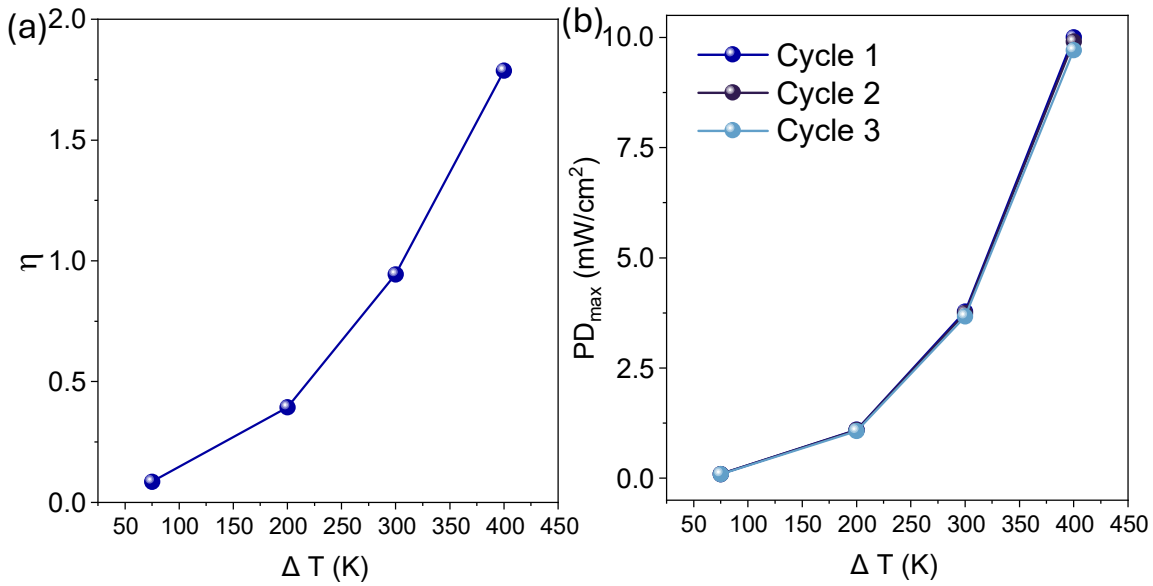


**Fig. S22.** (a) Estimated device efficiency (η) and (b) cyclability of output power density of single-leg thermoelectric device based on $Sn_{0.985}S$ at different temperature differences (ΔT).

**Table S1.** The elemental percentage obtained from EDAX spectra of the FESEM image of $Sn_{0.985}S$ in Fig. S5.

| Region | Atomic Percentage of Sn | Atomic Percentage of S |
|---|---|---|
| Region A | 49.2 | 50.8 |
| Region B | 34.2 | 65.8 |

**Table S2.** Grüneisen parameter and elastic properties of SnS and $Sn_{0.985}S$ estimated through sound velocity calculations.

| **Properties** | **SnS** | **$Sn_{0.985}S$** |
|---|---|---|
| Poisson's Ratio ($\nu$) | 0.251 | 0.286 |
| Grüneisen parameter ($\gamma$) | 1.50 | 1.69 |
| Bulk Modulus (B) | 38.68 GPa | 36.40 GPa |
| Shear Modulus (G) | 23.11 GPa | 18.10 GPa |

## References


1. R. Pathak, S. Paul, S. Das, A. Das, S. K. Pati and K. Biswas, *Angew. Chem. Int. Ed.*, 2024, **63**, e202408908.
2. A.-C. Dippel, H.-P. Liermann, J. T. Delitz, P. Walter, H. Schulte-Schrepping, O. H. Seeck and H. Franz, *J. Synchrotron Radiat.*, 2015, **22**, 675-687.
3. M. Basham, J. Filik, M. T. Wharmby, P. C. Y. Chang, B. El Kassaby, M. Gerring, J. Aishima, K. Levik, B. C. A. Pulford, I. Sikharulidze, D. Sneddon, M. Webber, S. S. Dhesi, F. Maccherozzi, O. Svensson, S. Brockhauser, G. Naray and A. W. Ashton, *J. Synchrotron Radiat.*, 2015, **22**, 853-858.
4. P. Juhas, T. Davis, C. L. Farrow and S. J. L. Billinge, *J. Appl. Crystallogr.*, 2013, **46**, 560-566.
5. C. L. Farrow, P. Juhas, J. W. Liu, D. Bryndin, E. S. Božin, J. Bloch, T. Proffen and S. J. L. Billinge, *J. Condens. Matter Phys.*, 2007, **19**, 335219.
6. P. Acharyya, S. Roychowdhury, M. Samanta and K. Biswas, *J. Am. Chem. Soc.*, 2020, **142**, 20502-20508.
7. S. Roychowdhury, T. Ghosh, R. Arora, M. Samanta, L. Xie, N. K. Singh, A. Soni, J. He, U. V. Waghmare and K. Biswas, *Science*, 2021, **371**, 722-727.
8. R. Chetty, Y. Kikuchi, Y. Bouyrie, P. Jood, A. Yamamoto, K. Suekuni and M. Ohta, *J. Mater Chem. C.*, 2019, **7**, 5184-5192.